Editors' Suggestion

Investigation of electrical and thermal transport property reductions in La-doped $BaSnO_3$ films

Hai Jun Cho,[1,2,*] Bin Feng,[3] Takaki Onozato,[1] Mian Wei,[1] Anup V. Sanchela,[1] Yuichi Ikuhara,[3] and Hiromichi Ohta[1,2,†]

[1]*Research Institute for Electronic Science, Hokkaido University, N20W10, Kita, Sapporo 001-0020, Japan*
[2]*Graduate School of Information Science and Technology, Hokkaido University, N14W9, Kita, Sapporo 060-0814, Japan*
[3]*Institute of Engineering Innovation, The University of Tokyo, 2-11-16 Yayoi, Bunkyo, Tokyo 113-8656, Japan*

(Received 13 May 2019; revised manuscript received 18 June 2019; published 3 September 2019)

The electron mobility value of 320 $cm^2\,V^{-1}\,s^{-1}$ observed from La-doped $BaSnO_3$ (LBSO) single crystals has a great potential in optoelectronic applications, but LBSO films exhibit much lower mobilities. Threading dislocations from the film/substrate mismatch are believed to be the main source of this phenomenon, but previous experiments suggest that they do not fully explain the mobility suppression. In this paper, we examined the thickness dependence of electrical and thermal transport properties of LBSO films fabricated in different oxidation environments. The results show that oxygen deficiency also affects the electron mobility of LBSO films, and the mobility suppression in LBSO films is dominated by different mechanisms depending on the thicknesses. LBSO films with different oxygen vacancy contents were fabricated using the pulsed laser deposition technique. The films deposited under higher oxidative conditions exhibited lower oxygen deficiency levels and superior transport properties whereas the threading dislocation densities remained unchanged. The highest mobility value observed in this paper was 120 $cm^2\,V^{-1}\,s^{-1}$, which is comparable to LBSO films fabricated on thick buffer layers. Our paper provides a broader perspective on understanding the mobility of LBSO films and confirms that threading dislocations are not the only factor.

DOI: 10.1103/PhysRevMaterials.3.094601

I. INTRODUCTION

La-doped $BaSnO_3$ (LBSO) is considered to be one of the leading candidates for the development of transparent electronic devices due to its large band gap (~3.5 eV) and high single-crystal electron mobility (μ_e) value of 320 $cm^2\,V^{-1}\,s^{-1}$ [1] at relatively high carrier concentrations of $\sim 10^{20}$ cm^{-3}, which is comparable to that of doped silicon (~350 $cm^2\,V^{-1}\,s^{-1}$) [2]. For this reason, there have been many attempts to build thin LBSO film transistors, but the observed mobilities have been significantly low compared to the single-crystal value [3–8]. Electron scatterings at threading dislocations are believed to be the main source of this mobility suppression, and most studies focused on eliminating the lattice mismatch at the film/substrate interface [4,6,8–10], which is the source of threading dislocations. Inserting a buffer layer at the LBSO/substrate interface is the most common approach [11,12], and Lee *et al.* even used single-crystal $BaSnO_3$ as the substrate to grow homoepitaxial LBSO films [13]. Unfortunately, although these approaches were successful in improving the electron mobility of LBSO films, the resulting μ_e values were still much lower than the single-crystal values, implying that the threading dislocations are not enough to fully explain the mobility suppression in LBSO films.

A previous study found that the μ_e of LBSO films fabricated by pulsed laser deposition (PLD) exhibits a very strong thickness dependence [14]. One can easily suspect that the thickness effect is attributed to the lattice strains from the film/substrate mismatch. However, the LBSO films on both MgO (001) and $SrTiO_3$ (001) substrates showed almost the same thickness-dependent μ_e values despite having significantly different lattice mismatches (MgO: −2.4%, $SrTiO_3$: +5.1%). This suggests a presence of another source of mobility suppression that is not related to the film/substrate lattice mismatch. One example of such factors can be point defects. For example, LBSO films grown from molecular beam epitaxy (MBE) tend to be more stoichiometric than those grown from PLD, and studies have shown that MBE-LBSO films (highest: ~183 $cm^2\,V^{-1}\,s^{-1}$ [3]) exhibit higher μ_e than PLD-LBSO films (highest: ~115 $cm^2\,V^{-1}\,s^{-1}$ [15]). Prakash *et al.* deliberately changed the Sn/Ba ratio in LBSO films and demonstrated that the μ_e varied from 1 to 100 $cm^2\,V^{-1}\,s^{-1}$ whereas the thermal conductivity (κ) changed from 1.89 to 13.3 $W\,m^{-1}\,K^{-1}$ [16]. Point defect formations in LBSO were more thoroughly investigated with *ab initio* calculations [17,18], and the results suggest that oxygen vacancies in LBSO can naturally occur in nonoxidative environments (i.e., low chemical potential for oxygen). Oxygen atoms in undoped $BaSnO_3$ have an excellent chemical stability [19], and undoped $BaSnO_3$ films exhibit low oxygen deficiency unless oxygen vacancies are intentionally created [20,21]. However, a recent study showed that La doping reduces the thermal stability of oxygen and increases the oxygen deficiency in LBSO films [22]. The thickness dependence, *ab initio* calculations, and experimental observation of oxygen vacancies show that improving the μ_e of LBSO films will involve understanding multiple factors. However, most studies are only concerned with eliminating threading dislocations,

*joon@es.hokudai.ac.jp
†hiromichi.ohta@es.hokudai.ac.jp

and there is a necessity for examining the mobility suppression in LBSO films from another perspective.

LBSO films are usually grown from vapor processes, such as PLD or MBE where the chemical potential of oxygen is controlled with the oxidation environment. The oxidation environment is usually adjusted with the oxygen (O_2) pressure in PLD [23] and ozone (O_3) pressure in MBE [24]. Since ozone creates much more oxidative environments compared to oxygen [25,26], oxygen vacancy formation in MBE-LBSO films will be suppressed compared to that in PLD-LBSO films, which may be related to the higher μ_e in reported in MBE-LBSO films. A recent study on PLD-fabricated LBSO films, indeed, showed that injecting O_3 during the deposition process enhances the μ_e values [15]. However, in Ref. [15], reduction in the oxygen deficiency from O_3 was only proposed as a plausible mechanism, and the oxygen deficiencies in the films fabricated with and without O_3 were not directly compared. Therefore, there is still a lack of studies that can shed light on the oxygen vacancy effect on the μ_e of LBSO films.

To clearly confirm the oxygen vacancy effect on the transport properties of the LBSO films, in-plane transport properties are not sufficient enough since they are affected by both oxygen vacancies and threading dislocations. In the through-plane direction, the oxygen vacancy effect can be isolated since the flux of energy in this case is parallel to threading dislocations. However, measuring the electrical transport properties across thin films is extremely challenging due to difficulties in making appropriate electrical contacts. For this reason, other through-plane transport properties that are sensitive to oxygen vacancies are required and thermal conductivity measurements can be of great value in this regard.

Unlike electrical transport properties, the thermal transport properties of thin films are commonly measured in the through-plane direction [27,28]. Since vibrational properties are affected by point defects, the oxygen deficiency in the film will be reflected in the through-plane thermal conductivity ($\kappa_\perp$). The $\kappa_\perp$ of an epitaxial $BaSnO_3$ film (350 nm) is very similar to the κ of a bulk $BaSnO_3$ single crystal [16,28], confirming that the $\kappa_\perp$ of thin films is, indeed, not strongly affected by threading dislocations. This implies that the $\kappa_\perp$ of epitaxial LBSO films may be used to qualitatively compare the oxygen deficiency levels, which can connect the LBSO film fabrication conditions (O_2 or O_3) with the resulting oxygen deficiency level and μ_e. Furthermore, understanding the thermal transport properties is also essential for controlling the heat dissipation in practical device applications. However, despite their significance, the through-plane thermal transport properties of epitaxial LBSO films have not been addressed in literature in detail.

In this paper, we examined the role of oxygen vacancies in the μ_e suppression in LBSO films. Epitaxial LBSO films with varying thicknesses from 30 to 500 nm were prepared on MgO substrates using PLD whereas the oxygen deficiency in the films was controlled with the partial pressure of O_3 during the film growth. X-ray photoelectron spectroscopy (XPS) confirmed that the O_3 environment removes oxygen vacancies in LBSO films. We compared the structural and transport properties of the LBSO films fabricated with pure oxygen (O_2 LBSO) and those fabricated with ozone (O_3 LBSO). In addition to μ_e and lattice strain, $\kappa_\perp$ was also affected by the film thickness, but the thickness gradient of all properties greatly changed with the injection of O_3 (Fig. 1). The structural characterizations indicate that the O_3 environment reduces the lattice strains and improves the crystallinity of LBSO films. The μ_e values of O_3-LBSO films were superior than those of O_2-LBSO films whereas the XPS spectra confirmed that the O_3-LBSO films exhibited lower oxygen deficiency. The $\kappa_\perp$ of the O_3-LBSO films was also greater than that of the O_2-LBSO films. All our results coherently suggest that the oxygen deficiency reduction in LBSO films can be achieved in strongly oxidative environments, which improves the μ_e of LBSO films. We believe these results will be of great value in clarifying the electron mobility suppression in LBSO films and building better LBSO film-based electronic devices. The thermal transport properties will also be valuable for device applications because they are directly associated with the heat dissipation, which is one of the major concerns in film transistors [29].

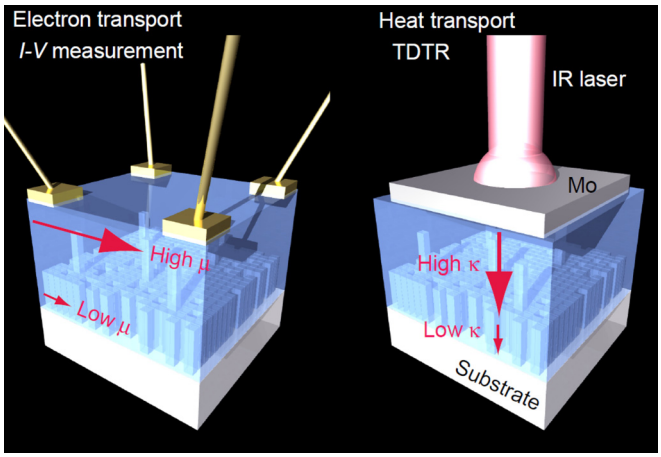

FIG. 1. The thickness dependence of the transport properties observed in this paper. All transport properties of LBSO films near the film/substrate interface are lower than those away from the interfaces. Studies on the point defect formations in LBSO films [17,18,22] suggest oxygen vacancies can also be related to the transport properties of LBSO films, and this paper, indeed, showed that the thickness gradient can be affected by the oxidation condition during the film deposition process.

II. EXPERIMENT

A. Film growth

Two percent doped LBSO ($La_{0.02}Ba_{0.98}SnO_3$) films were heteroepitaxially grown on (001) MgO single-crystal substrates by PLD (KrF excimer laser, $\lambda = 248$ nm, fluence $\sim 2\ \mathrm{J\,cm^{-2}\,pulse^{-1}}$, repetition rate = 10 Hz). The growth temperature was kept at 750 °C. For the deposition of O_2-LBSO films, the oxygen pressure was set to 10 Pa. On the other hand, for the deposition of O_3-LBSO films, the partial pressures of oxygen and ozone were 15.3 and 1.7 Pa (10% O_3), respectively.

B. Film characterizations

The crystallographic parameters of the LBSO films were analyzed by the high-resolution x-ray diffraction (Cu $K\alpha 1$, ATX-G, Rikaku Co.). The film thickness was determined from the Kiessing fringes in x-ray reflectivity (data not shown). The microstructures of the films were characterized with scanning transmission electron microscopy (STEM). The electrical conductivity (σ), electron density (n), and electron mobility (μ_e) of the LBSO films were measured at room temperature (RT) by the conventional DC four-probe method in van der Pauw geometry using a magnetic field of 7600 G. The oxygen content of the LBSO films was analyzed with XPS. The O 1s peaks were deconvoluted, and the areas of the lattice oxygen peak and the oxygen vacancy peak were compared. The thermal conductivity of the films was measured using time-domain thermoreflectance [(TDTR), probe laser wavelength = 775 nm, pump laser wavelength = 1550 nm, pulse frequency = 20 MHz, modulation frequency = 200 kHz, PicoTR, PicoTherm Corp.]. Sputtered Mo (thickness: ~100 nm) was used as the transducer, and the TDTR signal was analyzed with the TDTR simulation software package provided by the manufacturer (Supplemental Material Fig. S4 [30]).

III. RESULTS AND DISCUSSION

The oxygen 1s (O^{1s}) XPS spectra of O_2-LBSO (126-nm) and O_3-LBSO (140-nm) films are shown in Fig. 2. For the XPS fitting, a Gaussian (70%) Lorentzian (30%) mix was used, and the full widths at half maximum of the three different oxygen peaks were constrained to be the same. It seems that the XPS signals are composed of two peaks. However, if the two-peak fitting process is implemented, the secondary peak in O_3 LBSO shifts to the right (Supplemental Material Fig. S1 [30]), implying that it consists of, at least, two different peaks. In oxides, O^{1s} peaks can be deconvoluted into lattice oxygen (~529 eV), oxygen vacancy (~531 eV), and chemically adsorbed oxygen (~533 eV) [31–37]. Therefore, the secondary peak observed from the LBSO films in this paper is the convolution of the oxygen vacancy peak and the adsorbed oxygen peak. With the injection of O_3, the secondary peak shifted to the right, which implies the reduction of oxygen vacancy peak relative to the adsorption peak. Since the large adsorption peak makes the XPS analysis tricky, we implemented two different fitting procedures. At first, the peaks in O_2-LBSO and O_3-LBSO films were fitted independently [Figs. 2(a) and 2(c)]. In the second procedure, the peak widths of both O_2-LBSO and O_3-LBSO films were constrained to be the average width of the first procedure [Figs. 2(b) and 2(d)]. The peak locations were close to the reported values, and the relative distances between the peaks were reasonably preserved in both O_2-LBSO and O_3-LBSO films. All fitting results are summarized in Table I. In the independent fitting, the oxygen vacancy to the lattice oxygen ratio is greatly reduced in the O_3-LBSO film (0.47 → 0.24). The difference in the oxygen vacancy peak is suppressed when the additional constraint was imposed in the second fitting procedure, but the O_3 films still exhibited a lower (oxygen vacancy)/(lattice oxygen) ratio (0.39 → 0.34). Both fitting procedures show

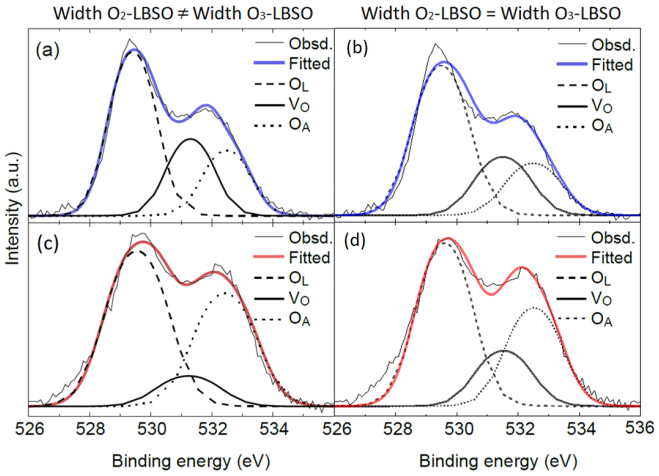

FIG. 2. Oxygen 1s XPS spectrum of (a) and (b) 126-nm-thick O_2-LBSO and (c) and (d) 140-nm-thick O_3-LBSO films. The peaks are deconvoluted into lattice oxygen (O_L), oxygen vacancy (V_O), and adsorbed oxygen (O_A). The oxygen vacancy peak is attributed to the oxygen atoms adjacent to oxygen vacancies, and the adsorption peak is attributed to surface contaminations by organic molecules (i.e., oxidized hydrocarbon, adsorbed water). If O_2 LBSO and O_3 LBSO are fitted independently (a) and (c), the oxygen vacancy peak is significantly reduced. If the peak widths of O_2 LBSO and O_3 LBSO are constrained to be the same, the difference in the oxygen vacancy peak is suppressed, but the O_3-LBSO film still exhibits a smaller V_O/O_L ratio (Table I).

that the ozone environment successfully reduced the oxygen deficiency in the LBSO films.

Examples of STEM performed on the LBSO films are shown in Fig. 3. For both the O_2-LBSO and the O_3-LBSO films, the STEM micrographs from the film/substrate interfaces reveal coherent interfaces with occasional misfit dislocations (Supplemental Material Fig. S2 [30]), suggesting the films are fully relaxed. According to the micrographs, the oxidation environment during the synthesis did not

TABLE I. XPS characteristics of O_2-LBSO and O_3-LBSO films. From low energy to high energy, the peaks are as follows: lattice oxygen, oxygen vacancy, and adsorbed oxygen. The peak areas were normalized with respect to the lattice oxygen peak.

Width O_2-LBSO ≠ O_3-LBSO			
O_2-LBSO peak locations	529.4 eV	531.3 eV	532.5 eV
O_2-LBSO peak widths	0.7 eV	0.7 eV	0.7 eV
O_2-LBSO peak areas	1	0.47	0.37
O_3-LBSO locations	529.5 eV	531.4 eV	532.5 eV
O_3-LBSO peak widths	0.9 eV	0.9 eV	0.9 eV
O_3-LBSO peak areas	1	0.24	0.69
Width O_2-LBSO = O_3-LBSO			
O_2-LBSO peak locations	529.5 eV	531.5 eV	532.5 eV
O_2-LBSO peak widths	0.8 eV	0.8 eV	0.8 eV
O_2-LBSO peak areas	1	0.39	0.35
O_3-LBSO locations	529.6 eV	531.5 eV	532.5 eV
O_2-LBSO peak widths	0.8 eV	0.8 eV	0.8 eV
O_3-LBSO peak areas	1	0.34	0.60

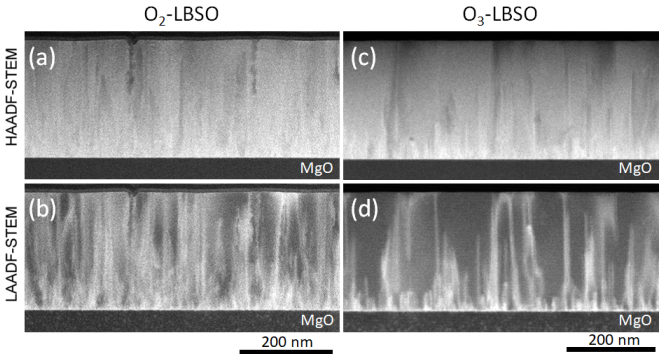

FIG. 3. STEM micrographs of the LBSO films. (a) HAADF-STEM and (b) LAADF-STEM micrographs of a 250-nm O_2-LBSO film. (c) HAADF-STEM and (d) LAADF-STEM micrographs STEM of a 270-nm O_3-LBSO film. Near the film/substrate interface, the LAADF contrast of O_3-LBSO films is slightly lower than that of O_2-LBSO films. However, the LAADF contrast away from the interface is drastically lower in the O_3-LBSO films. This shows that highly oxidative atmospheres greatly reduced the lattice strains in the film.

affect the quality of interfaces, which implies that the physical property discrepancies between O_2-LBSO and O_3-LBSO films are related to the intrinsic properties of the films. On the other hand, interesting differences can be observed from annular dark-field micrographs. Although the high-angle annular dark-field (HAADF) micrographs do not show significant distinctions, the low-angle annular dark-field (LAADF) contrasts are significantly lower in O_3-LBSO films compared to O_2-LBSO films. Since the LAADF contrast contains the information of strain [38,39], the micrographs suggest that the lattice of the O_3-LBSO film is much more relaxed compared to that of the O_2-LBSO film, especially away from the interface. Despite the drastic difference in strain, the microstructures of O_2-LBSO and O_3-LBSO films were nearly identical, and the vertical stripes in LAADF micrographs are not necessarily attributed to threading dislocations (Supplemental Material Fig. S2 [30]).

The lattice characteristics of the LBSO films obtained from the x-ray reciprocal space mapping (RSM) are summarized in Fig. 4. The diffraction spots from LBSO (204) became more intense and narrower as the film thickness increased (Supplemental Material Table S1, Fig. S3 [30]), which implies that the crystallinity of the LBSO films improves with the thickness. Regardless of the oxidation conditions, the lattice constants gradually formed plateaus with increasing thickness. Initially, at low thicknesses, the in-plane lattice parameter (*a* axis) and the out-of-plane lattice parameter (*c* axis) of the LBSO films are in tension and compression, respectively. This is reasonable since the lattice parameter of MgO (4.212 Å) is higher that of $BaSnO_3$ (4.115 Å). Although the *c* axes of O_2-LBSO and O_3-LBSO films were similar, the most noticeable changes due to the oxidation condition can be observed from the *a* axis. In the case of O_2-LBSO films, the *a* axis is under tension at the beginning but eventually becomes compressed as the thickness increases. In contrast, the *a* axis of O_3-LBSO films is under higher tension compared to O_2-LBSO films at the beginning, but it

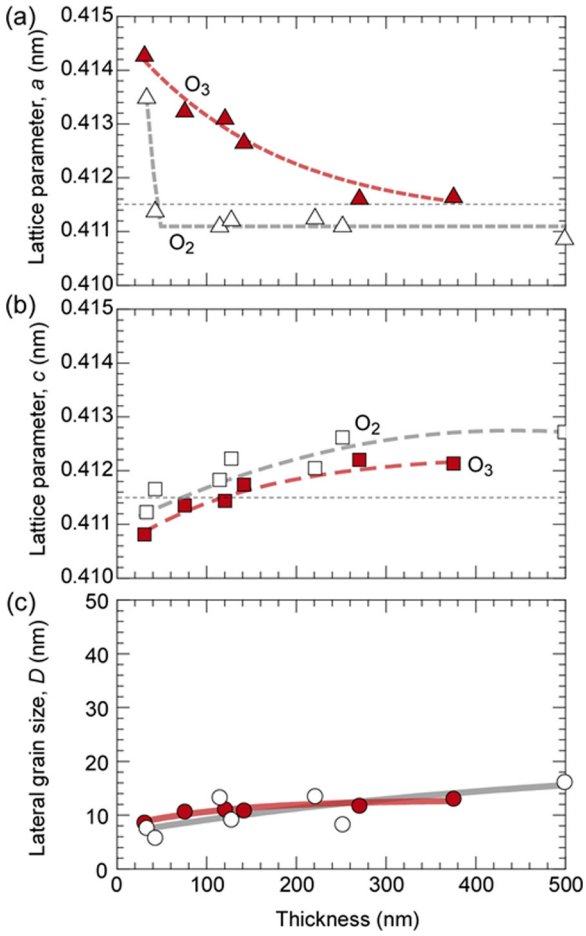

FIG. 4. Lattice characteristics of the LBSO films. (a) In-plane (*a*-axis) lattice constants of LBSO films. (b) Out-of-plane (*c*-axis) lattice constants of LBSO films. (c) The lateral grain sizes of the LBSO films calculated by Scherrer's equation, which represent the threading dislocation densities. The uncertainty in the lattice parameters is 0.0005 nm, which comes from the bin size of the RSMs (bin size$\times$10). At small thicknesses, O_2-LBSO films have lower lattice strains compared to O_3-LBSO films. However, as the films become thicker, the lattice strains in O_3-LBSO films become smaller than those in O_2-LBSO films.

approaches the exact bulk value as the films grow thicker. The lattice relaxation rates also differ. The *a* axis of O_2 LBSO quickly reaches a plateau at $\sim$100 nm, which is similar with a previous study on sputtered $BaSnO_3$ on the MgO (001) substrate [20]. On the other hand, the relaxation of the *a* axis of O_3-LBSO films is more gradual, which resembles the evolution of lattice constants of the undoped $BaSnO_3$ buffer film [11]. The lattice constant patterns observed from Figs. 4(a) and 4(b) show that the O_3 environment changes the linear strain after relaxation as well as the relaxation rate, which is consistent with the LAADF micrographs. The lateral grain size (*D*) of the films, calculated using the RSM peak coherence length and Scherrer's equation [i.e., grain size=lateral coherence length=(integration width)$^{-1}$] [14], increased with the film thickness. Despite the grain size fluctuations observed in O_2-LBSO films, the guide-to-eye lines did not exhibit a strong dependence on the oxidation

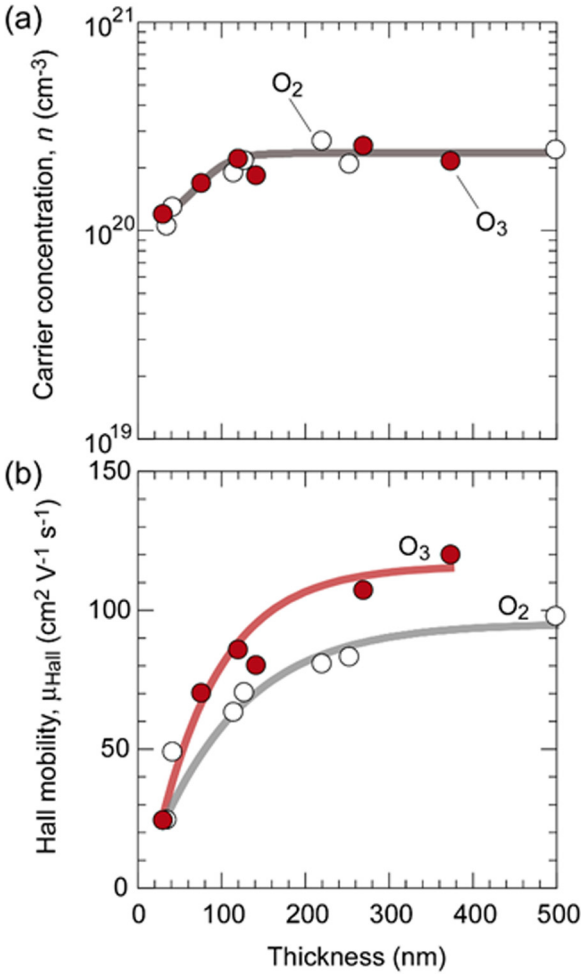

FIG. 5. Electron transport properties of LBSO films fabricated in O_2 and O_3 atmospheres. (a) Carrier concentration n against the film thickness. (b) Hall mobility μ_{Hall} ($= \mu_e$) against the film thickness. The μ_{Hall} of the O_3-LBSO films are always greater than that of the O_2-LBSO films.

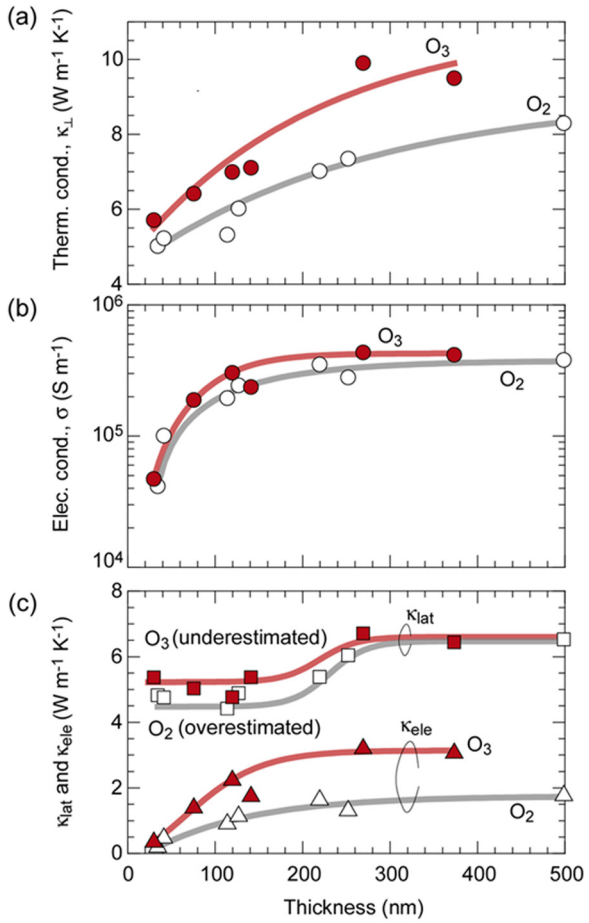

FIG. 6. (a) Observed through-plane thermal conductivity ($\kappa_\perp$) at RT. The $\kappa_\perp$ of the O_3-LBSO films are always greater than that of O_2-LBSO films. (b) Electrical conductivity (σ) of the LBSO films at RT. (c) Estimated electron and lattice thermal conductivities of LBSO films. The electron thermal conductivities for O_2-LBSO films were underestimated ($L = 1.5 \times 10^{-8}\ \mathrm{W^{-1}\,\Omega^{-1}\,K^2}$) whereas those for O_3-LBSO films were overestimated ($L = 2.45 \times 10^{-8}\ \mathrm{W^{-1}\Omega^{-1}\,K^2}$). Although a higher Lorenz number was chosen for O_3-LBSO films, they still show higher κ_{lat} compared to O_2-LBSO films.

condition. This suggests that the oxidation condition did not strongly affect the threading dislocation density. Despite having higher strains at low thicknesses, the diffraction spot of O_3-LBSO films was more intense compared to that of O_2-LBSO films (Supplemental Material Fig. S3 [30]). Since oxygen vacancies reduce the XRD intensity [40], this indicates that the oxygen deficiency level of O_3-LBSO films is lower than that of O_2-LBSO films. In addition, the intensity difference was not strong at small thicknesses, but it gradually increased as the films became thicker. This shows that the effect of ozone near the film/substrate interface is not as strong as that away from the interface, which implies that oxygen vacancies in LBSO films may have higher stability near the interface. All structural characterizations suggest that the oxidation environment during the film growth changed the bulk lattice of the LBSO films.

The transport properties of the LBSO films are summarized in Figs. 5 and 6. All transport properties increase with the film thickness, which agrees with the crystallinity enhancements observed from the structural characterizations. At very small thicknesses, the transport properties of O_2-LBSO and O_3-LBSO films were similar. As the films became thicker, the transport properties of O_2-LBSO films reached $\kappa_\perp \sim 8\ \mathrm{W/mK}$ and $\mu_e \sim 98\ \mathrm{cm^2\,V^{-1}\,s^{-1}}$ whereas those of O_3-LBSO films saturated at $\kappa_\perp \sim 10\ \mathrm{W/mK}$ and $\mu_e \sim 120\ \mathrm{cm^2\,V^{-1}\,s^{-1}}$. In general, films with higher μ_e also showed higher $\kappa_\perp$, and O_3-LBSO films exhibited greater thermal and electrical transport properties compared to O_2-LBSO films [Figs. 5(a) and 6(a)]. We would like to note that the best mobility value in this paper ($120\ \mathrm{cm^2\,V^{-1}\,s^{-1}}$) is comparable to or even higher than the μ_e of LBSO films with buffer layers [11,12]. These results demonstrate the electron mobility suppression in LBSO films can be lifted without significantly reducing the threading dislocation density by changing the film growth atmosphere, which indicate that threading dislocations are not the only source of mobility suppression.

The conduction of heat in degenerate semiconductors, such as LBSO can be divided into the lattice thermal conductivity

(κ_{lat}) and the electron thermal conductivity (κ_{ele}). As the O_3-LBSO films have better electron transport properties, it is not difficult to see that κ_{ele} of O_3-LBSO films would be greater than that of O_2-LBSO films. Therefore, to clearly demonstrate the oxygen deficiency effect on the heat transport properties, κ_{lat} must be isolated from the measured $\kappa_\perp$ ($= \kappa_{lat} + \kappa_{ele}$). κ_{ele} can be estimated with the Wiedemann-Franz law [41],

$$\kappa_{ele} = L\sigma T, \tag{1}$$

where T is the temperature and L is the Lorenz number. In the case of single band semiconductors, such as LBSO [42], L can vary from 1.5×10^{-8} to 2.45×10^{-8} W Ω K^{-2} [43]. The 2.45×10^{-8} W Ω K^{-2} is also the Lorenz number for a free electron gas, which works very well for metals. For this reason, 2.45×10^{-8} W Ω K^{-2} is often used as the upper bound for κ_{ele}. Figure 6(c) shows overestimated κ_{lat} for O_2-LBSO films ($L = 1.5 \times 10^{-8}$ W Ω K^{-2}) and underestimated κ_{lat} for O_3-LBSO films ($L = 2.45 \times 10^{-8}$ W Ω K^{-2}). Although we intentionally used different values of L to minimize the difference between κ_{lat} of O_2-LBSO and O_3-LBSO films, the κ_{lat} of O_3-LBSO films is still higher, confirming they, indeed, have low lattice defects compared to O_2-LBSO films. Since the microstructures of O_2-LBSO and O_3-LBSO films are essentially the same (Fig. S2 of the Supplemental Material [30]), the difference in their thermal conductivity is related to point defects, which is likely related to the oxygen deficiency (Fig. 2).

The thermal conductivity of thin films usually increases monotonically with the thickness [44–48]. However, the calculated κ_{lat} values in Fig. 6(c) exhibit very strange patterns. This suggests that the Wiedemann-Franz law does not adequately describe the heat transport properties of conduction electrons in LBSO, and we believe this highlights the necessity for better understanding on κ_{ele} of oxides. In fact, studies have addressed the failure of the Wiedemann-Franz law theoretically [49] and experimentally [50]. For example, the Wiedemann-Franz law assumes a high T_D/T ratio ($T_D =$ Debye temperatures) [41,51,52], but the Debye temperature of $BaSnO_3$ (307 K [42]) is not very high compared to the room temperature. The thermal conductivity of undoped $BaSnO_3$ was reported to be ∼13 W m^{-1} K^{-1} for a bulk single crystal as well as a 350-nm-thick film [16,28]. Since the observed $\kappa_\perp$ values (5.0–9.9 W m^{-1} K^{-1}) are lower than the undoped single-crystal values, the real contribution from κ_{ele} is likely not significant, and the thermal conductivity difference between O_2-LBSO and O_3-LBSO films can be attributed to the reduction of oxygen deficiency.

It is interesting to note that the n's of O_2-LBSO and O_3-LBSO films are very similar since oxygen vacancies in $BaSnO_3$ create mobile electrons [20,21]. Like many other studies [3–8], the carrier concentrations of all LBSO films in our paper are noticeably below the [La^{3+}] doping concentration (2.87×10^{20} cm^{-3}), suggesting the presence of charge compensating defects [16]. According to Weston *et al.*, two of the charge accepting point defects in LBSO with the lowest formation energies are the La occupying Sn site (La_{Sn}) and the Ba vacancy (V_{Ba}). As the Fermi energy shifts toward the conduction-band minimum with increasing carrier density, the concentration of these defects increases as their formation energies are reduced [18]. If oxygen deficiencies are reduced with the injection of O_3, the formation energy and the concentration of the charge accepting point defects would decrease, and some of the carrier electron loss will be compensated. It is also possible that the injection of O_3 improves the stoichiometry of the film and suppresses the formation of La_{Sn} and V_{Ba}, which can be related to the drastic strain reduction in the O_3-LBSO films (Fig. 3). The *ab initio* calculation also shows that Ba-rich LBSO exhibits lower charge compensating defects compared to Sn-rich LBSO [18]. In our experiment, the energy dispersive x-ray spectroscopy (EDS) of the LBSO films, indeed, shows that the Ba:Sn ratio in O_2-LBSO films is 0.99:1.00 whereas that of the O_3-LBSO films is 1.01:1.00 (error: 0.002, Supplemental Material Fig. S5 [30]).

Although *ab initio* studies provide a great insight for understanding the point defects in LBSO, they are limited to bulk single crystals due to limitations in computational power. Previous experimental studies show that there is a relationship between structural defects and point defects in LBSO films. For example, insulating undoped $BaSnO_3$ films can be doped with oxygen vacancy after vacuum annealing, which greatly increases the electron density [20,21]. However, a previous study on unintentionally oxygen vacancy doped $BaSnO_{3-\delta}$ single crystals showed that the electron-density change after vacuum annealing is almost negligible compared to thin films [53]. The origin of this discrepancy is not clear, but it is likely related to the microstructure defects associated with thin films. In the case of La-doped $BaSnO_3$ films, the La dopant serves as another factor since a recent study found that oxygen deficiency increases with La dopants [22]. Threading dislocations in semiconductor films are known to promote vacancies [54–56], and some studies utilized this phenomenon to induce lateral grain growths in LBSO [22,57,58]. For these reasons, understanding the interaction among substrate dangling bonds, threading/misfit dislocations, La dopants, and oxygen atoms is crucial. However, it is beyond the scope of our current paper, and we would like to address it in detailed future studies.

This paper explored sources of μ_e suppression in LBSO films other than threading dislocations and showed that oxygen vacancies are an important factor as well. Once the threading dislocations are eliminated, *ab initio* calculations predict that the μ_e will then be limited by electron scatterings from longitudinal optical phonons [12]. However, this calculation was performed on bulk LBSO single crystals and, therefore, may not adequately represent thin films. For instance, our $\kappa_\perp$ values [Fig. 6(a)] indicate that the vibrational properties of LBSO films depend on the thickness, suggesting that electron-phonon scattering cross-sectional areas in LBSO films can be different from those in single crystals. In addition, boundary scatterings are not negligible in thin films. Consequently, the ideal μ_e of LBSO films may be different from that of LBSO bulk single crystals. The LBSO transport properties measured in this paper imply that the films exhibit a thickness gradient where a low-transport region is accumulated at the film/substrate interface. For 30-nm films, O_2 LBSO and O_3 LBSO showed the same μ_e, but the $\kappa_\perp$ of O_3 LBSO was ∼14% higher than that of O_2 LBSO. This suggests that the mobility suppression at the film/substrate interface is not significantly affected by the oxygen vacancies but dominated

by other factors, such as the lattice mismatch, lattice strain, and changes in electron-phonon collisions. Between ∼30 and ∼300 nm, the effects from the interface are reduced, and μ_e seems to be mainly dependent on both the threading dislocations and the oxygen vacancies. Above ∼300 nm, increasing the lateral grain size and eliminating the threading dislocations no longer increases μ_e, and μ_e enhancements can only be achieved from further eliminating the oxygen deficiency, which also reduced the lattice strains (Figs. 3, 5, and 6).

The upshot of all studies on the electrical properties of LBSO films is achieving the single-crystal mobility (320 $cm^2\ V^{-1}\ s^{-1}$) at a reasonable cost for commercialization. Although epitaxial LBSO films from PLD or MBE exhibit excellent film qualities and transport characteristics, they require incredibly specialized costly equipment, and cost reduction will be a critical issue for large-scale production facilities. As we search for more economical tools for fabricating LBSO films, our paper suggests that preserving the stoichiometry, especially reducing the oxygen vacancy formation, can be just as important as eliminating threading dislocations or grain boundaries.

IV. CONCLUSIONS

To summarize, we investigated the role of oxygen vacancies in the electron mobility suppression in LBSO films. We fabricated epitaxial LBSO films on MgO (001) substrates under two different oxidation conditions: pure O_2 and 10% O_3 environments. The structural characterizations and O^{1s} XPS spectra from the films showed that the O_3 environment reduced the oxygen deficiency level in the LBSO films. The O_3-LBSO films exhibited superior electron mobilities and thermal conductivities compared to the O_2-LBSO films. According to these results, electron scattering at threading dislocations is not the only source of mobility suppression in LBSO films, and understanding oxygen vacancy formation in LBSO films is of great importance in improving the electron mobility of LBSO films. We believe that the transport properties of LBSO films presented in this paper will be of great value for practical aspects in developing LBSO film devices, such as operation speed (μ_e) and heat dissipation ($\kappa_\perp$).

ACKNOWLEDGMENTS

This research was supported by Grants-in-Aid for Innovative Areas (19H05791) and Scientific Research A (17H01314) from the JSPS. H.J.C. acknowledges the support from Nippon Sheet Glass Foundation for Materials Science and Engineering. H.O. acknowledges the support from the Asahi Glass Foundation and the Mitsubishi Foundation. A part of this work was supported by the "Nanotechnology Platform" (12024046) of the Ministry of Education, Culture, Sports, Science and Technology (MEXT), Japan (B.F. and Y.I.). Student aids from the JSPS (T.O.) (17J01281) and the China Scholarship Council (M.W.) are also greatly appreciated. A part of this work was also supported by Dynamic Alliance for Open Innovation Bridging Human, Environment, and Materials, and by the Network Joint Research Center for Materials and Devices.

The authors declare no competing financial interest.

[1] H. Kim, U. Kim, H. Kim, T. Kim, H. Mun, B.-G. Jeon, K. Hong, W.-J. Lee, C. Ju, K. Kim, and K. Char, High mobility in a stable transparent perovskite oxide, Appl. Phys. Express **5**, 061102 (2012).

[2] N. M. Johnson, C. Herring, and D. J. Chadi, Interstitial Hydrogen and Neutralization of Shallow-Donor Impurities in Single-Crystal Silicon, Phys. Rev. Lett. **56**, 769 (1986).

[3] H. Paik, Z. Chen, E. Lochocki, A. Seidner, H. Verma, N. Tanen, J. Park, M. Uchida, S. Shang, B.-C. Zhou, M. Brützam, R. Uecker, Z.-K. Liu, D. Jena, K. M. Shen, D. A. Muller, and D. G. Schlom, Adsorption-controlled growth of La-doped $BaSnO_3$ by molecular-beam epitaxy, APL Mater. **5**, 116107 (2017).

[4] S. Raghavan, T. Schumann, H. Kim, J. Y. Zhang, T. A. Cain, and S. Stemmer, High-mobility $BaSnO_3$ grown by oxide molecular beam epitaxy, APL Mater. **4**, 016106 (2016).

[5] Z. Lebens-Higgins, D. O. Scanlon, H. Paik, S. Sallis, Y. Nie, M. Uchida, N. F. Quackenbush, M. J. Wahila, G. E. Sterbinsky, D. A. Arena, J. C. Woicik, D. G. Schlom, and L. F. Piper, Direct Observation of Electrostatically Driven Band Gap Renormalization in a Degenerate Perovskite Transparent Conducting Oxide, Phys. Rev. Lett. **116**, 027602 (2016).

[6] P. V. Wadekar, J. Alaria, M. O'Sullivan, N. L. O. Flack, T. D. Manning, L. J. Phillips, K. Durose, O. Lozano, S. Lucas, J. B. Claridge, and M. J. Rosseinsky, Improved electrical mobility in highly epitaxial La:$BaSnO_3$ films on $SmScO_3$ (110) substrates, Appl. Phys. Lett. **105**, 052104 (2014).

[7] C. A. Niedermeier, S. Rhode, S. Fearn, K. Ide, M. A. Moram, H. Hiramatsu, H. Hosono, and T. Kamiya, Solid phase epitaxial growth of high mobility La:$BaSnO_3$ thin films co-doped with interstitial hydrogen, Appl. Phys. Lett. **108**, 172101 (2016).

[8] U. Kim, C. Park, T. Ha, R. Kim, H. S. Mun, H. M. Kim, H. J. Kim, T. H. Kim, N. Kim, J. Yu, K. H. Kim, J. H. Kim, and K. Char, Dopant-site-dependent scattering by dislocations in epitaxial films of perovskite semiconductor $BaSnO_3$, APL Mater. **2**, 056107 (2014).

[9] H. Mun, U. Kim, H. M. Kim, C. Park, T. H. Kim, H. J. Kim, K. H. Kim, and K. Char, Large effects of dislocations on high mobility of epitaxial perovskite $Ba_{0.96}La_{0.04}SnO_3$ films, Appl. Phys. Lett. **102**, 252105 (2013).

[10] Z. Wang, H. Paik, Z. Chen, D. A. Muller, and D. G. Schlom, Epitaxial integration of high-mobility La-doped BaSnO3 thin films with silicon, APL Mater. **7**, 022520 (2019).

[11] J. Shiogai, K. Nishihara, K. Sato, and A. Tsukazaki, Improvement of electron mobility in La:$BaSnO_3$ thin films by insertion of an atomically flat insulating (Sr, Ba)SnO_3 buffer layer, AIP Adv. **6**, 065305 (2016).

[12] A. Prakash, P. Xu, A. Faghaninia, S. Shukla, J. W. Ager, C. S. Lo, and B. Jalan, Wide bandgap $BaSnO_3$ films with room temperature conductivity exceeding 10^4 Scm^{-1}, Nat. Commun. **8**, 15167 (2017).

[13] W. Lee, H. J. Kim, E. Sohn, T. H. Kim, J. Park, W. Park, H. Jeong, T. Lee, J. H. Kim, K. Choi, and K. H. Kim, Enhanced

electron mobility in epitaxial (Ba, La)SnO_3 films on $BaSnO_3$ (001) substrates, Appl. Phys. Lett. **108**, 082105 (2016).

[14] A. Sanchela, M. Wei, H. Zensyro, B. Feng, J. Lee, G. Kim, H. Jeen, Y. Ikuhara, and H. Ohta, Large thickness dependence of the carrier mobility in a transparent oxide semiconductor, La-doped $BaSnO_3$, Appl. Phys. Lett. **112**, 232102 (2018).

[15] A. V. Sanchela, M. Wei, J. Lee, G. Kim, H. Jeen, B. Feng, Y. Ikuhara, H. J. Cho, and H. Ohta, Buffer layer-less fabrication of high-mobility transparent oxide semiconductor, La-doped $BaSnO_3$, J. Mater. Chem. C **7**, 5797 (2019).

[16] A. Prakash, P. Xu, X. Wu, G. Haugstad, X. Wang, and B. Jalan, Adsorption-controlled growth and the influence of stoichiometry on electronic transport in hybrid molecular beam epitaxy-grown $BaSnO_3$ films, J. Mater. Chem. C **5**, 5730 (2017).

[17] D. Scanlon, Defect engineering of $BaSnO_3$ for high-performance transparent conducting oxide applications, Phys. Rev. B **87**, 161201(R) (2013).

[18] L. Weston, L. Bjaalie, K. Krishnaswamy, and C. G. Van de Walle, Origins of n-type doping difficulties in perovskite stannates, Phys. Rev. B **97**, 054112 (2018).

[19] W. Lee, H. Kim, J. Kang, D. Jang, T. Kim, J. Lee, and K. Kim, Transparent perovskite barium stannate with high electron mobility and thermal stability, Annu. Rev. Mater. Res. **47**, 391 (2017).

[20] K. Ganguly, P. Ambwani, P. Xu, J. S. Jeong, K. A. Mkhoyan, C. Leighton, and B. Jalan, Structure and transport in high pressure oxygen sputter-deposited $BaSnO_{3-\delta}$, APL Mater. **3**, 062509 (2015).

[21] K. Ganguly, A. Prakash, B. Jalan, and C. Leighton, Mobility-electron density relation probed via controlled oxygen vacancy doping in epitaxial $BaSnO_3$, APL Mater. **5**, 056102 (2017).

[22] H. Cho, T. Onozato, M. Wei, A. Sanchela, and H. Ohta, Effects of vacuum annealing on the electron mobility of epitaxial La-doped $BaSnO_3$ films, APL Mater. **7**, 022507 (2019).

[23] R. Eason, *Pulsed Laser Deposition of Thin Films* (Wiley, Hoboken, NJ, 2007).

[24] M. Tsai, M. White, and J. Speck, Investigation of (110) SnO_2 growth mechanisms on TiO_2 substrates by plasma-assisted molecular beam epitaxy, J. Appl. Phys. **106**, 024911 (2009).

[25] L. Wang, P. Chu, A. Anders, and N. Cheung, Effects of ozone oxidation on interfacial and dielectric properties of thin HfO_2 films, J. Appl. Phys. **104**, 054117 (2008).

[26] C. Fink, K. Nakamura, S. Ichimura, and S. Jenkins, Silicon oxidation by ozone, J. Phys.: Condens. Matter **21**, 183001 (2009).

[27] D. Cahill, Analysis of heat flow in layered structures for time-domain thermoreflectance, Rev. Sci. Instrum. **75**, 5119 (2004).

[28] H. J. Kim, T. H. Kim, W.-J. Lee, Y. Chai, J. W. Kim, Y. J. Jwa, S. Chung, S. J. Kim, E. Sohn, S. M. Lee, K.-Y. Choi, and K. H. Kim, Determination of temperature-dependent thermal conductivity of a $BaSnO_{3-\delta}$ single crystal by using the 3ω method, Thermochim. Acta **585**, 16 (2014).

[29] S. G. Kandlikar, Review and projections of integrated cooling systems for three-dimensional integrated circuits, J. Electron. Packag. **136**, 024001 (2014).

[30] See Supplemental Material at http://link.aps.org/supplemental/10.1103/PhysRevMaterials.3.094601 for the data tables, STEM micrographs, RSM patterns, TDTR simulation, and EDS analysis.

[31] M. Ishfaq, M. Khan, M. Bhopal, F. Nasim, A. Ali, A. Bhatti, I. Ahmed, S. Bhardwaj, and C. Cepek, 1.5 MeV proton irradiation effects on electrical and structural properties of TiO_2/n-Si interface, J. Appl. Phys. **115**, 174506 (2014).

[32] F. Lei, Y. Sun, K. Liu, S. Gao, L. Liang, B. Pan, and Y. Xie, Oxygen vacancies confined in ultrathin Indium Oxide porous sheets for promoted visible-light water splitting, J. Am. Chem. Soc. **136**, 6826 (2014).

[33] J. Zheng, Q. Jiang, and J. Lian, Synthesis and optical properties of flower-like ZnO nanorods by thermal evaporation method, Appl. Surf. Sci. **257**, 5083 (2011).

[34] X.-G. Han, H.-Z. He, Q. Kuang, X. Zhou, X.-H. Zhang, T. Xu, Z.-X. Xie, and L.-S. Zheng, Controlling morphologies and tuning the related properties of nano/microstructured ZnO crystallites, J. Phys. Chem. C **113**, 584 (2009).

[35] D. Chen, F. Niu, L. Qin, S. Wang, N. Zhang, and Y. Huang, Defective $BiFeO_3$ with surface oxygen vacancies: facile synthesis and mechanism insight into photocatalytic performance, Sol. Energy Mater. Sol. Cells **171**, 24 (2017).

[36] A. F. Lee, J. N. Naughton, Z. Liu, and K. Wilson, High-pressure XPS of crotyl alcohol selective oxidation over metallic and oxidized Pd(111), ACS Catal. **2**, 2235 (2012).

[37] D. Briggs, D. M. Brewis, R. H. Dahm, and I. W. Fletcher, Analysis of the surface chemistry of oxidized polyethylene: comparison of XPS and ToF-SIMS, Surf. Interface Anal. **35**, 156 (2003).

[38] P. Phillips, M. De Graef, L. Kovarik, A. Agrawal, W. Windl, and M. Mills, Atomic-resolution defect contrast in low angle annular dark-field STEM, Ultramicroscopy **116**, 47 (2012).

[39] Z. Yu, D. Muller, and J. Silcox, Study of strain fields at a-Si/c-Si interface, J. Appl. Phys. **95**, 3362 (2004).

[40] J. D. Makinson, J. S. Lee, S. H. Magner, R. J. De Angelis, W. N. Weins, and A. S. Hieronymus, X-ray diffraction signatures of defects in nanocrystalline materials, Adv. X-Ray Anal. **42**, 407 (2000).

[41] C. Kittel, *Introduction to Solid State Physics* (Wiley, Hoboken, NJ, 2005).

[42] H. J. Kim, U. Kim, T. H. Kim, J. Kim, H. M. Kim, B.-G. Jeon, W.-J. Lee, H. S. Mun, K. Hong, J. Yu, K. Char, and K. H. Kim, Physical properties of transparent perovskite oxides (Ba, La)SnO_3 with high electrical mobility at room temperature, Phys. Rev. B **86**, 165205 (2012).

[43] L.-D. Zhao, S.-H. Lo, J. He, H. Li, K. Biswas, J. Androulakis, C.-I. Wu, T. P. Hogan, D.-Y. Chung, V. P. Dravid, and M. G. Kanatzidis, High performance thermoelectrics from earth-abundant materials: enhanced figure of merit in PbS by second phase nanostructures, J. Am. Chem. Soc. **133**, 20476 (2011).

[44] J. Reifengerga, M. Panzer, S. Kim, A. Gibby, Y. Zhang, S. Wong, H.-S. Wong, E. Pop, and K. Goodson, Thickness and stoichiometry dependence of the thermal conductivity of GeSbTe films, Appl. Phys. Lett. **91**, 111904 (2007).

[45] E. Ziade, J. Yang, G. Brummer, D. Nothern, T. Moustakas, and A. J. Schmidt, Thickness dependent thermal conductivity of gallium nitride, Appl. Phys. Lett. **110**, 031903 (2017).

[46] W. Zhu, G. Zheng, S. Cao, and H. He, Thermal conductivity of amorphous SiO_2 thin flm: A molecular dynamics study, Sci. Rep. **8**, 10537 (2018).

[47] S. Jeon, H. Shin, Y. Jaung, J. Ahn, and J. Song, Thickness-dependent and anisotropic thermal conductivity of black phosphorus nanosheets, Nanoscale **10**, 5985 (2018).

[48] W. Jang, Z. Chen, W. Bao, C. Lau, and C. Dames, Thickness-dependent thermal conductivity of encased graphene and ultrathin graphite, Nano Lett. **10**, 3909 (2010).

[49] M. Vavilov and A. Stone, Failure of the Wiedemann-Franz law in mesoscopic conductors, Phys. Rev. B **72**, 205107 (2005).

[50] S. Lee, K. Hippalgaonkar, F. Yang, J. Hong, C. Ko, J. Suh, K. Liu, K. Wang, J. J. Urban, X. Zhang, C. Dames, S. A. Hartnoll, O. Delaire, and J. Wu, Anomalously low electronic thermal conductivity in metallic vanadium dioxide, Science **355**, 371 (2017).

[51] D. Rowe and C. Bhandari, *Modern Thermoelectrics* (Reston, Reston, VA, 1983).

[52] W.-S. Liu, Q. Zhang, Y. Lan, S. Chen, X. Yan, Q. Zhang, H. Wang, D. Wang, G. Chen, and Z. Ren, Thermoelectric property studies on Cu-doped n-type $Cu_xBi_2Te_{2.7}Se_{0.3}$ nanocomposites, Adv. Energy Mater. **1**, 577 (2011).

[53] E. McCalla, D. Phelan, M. J. Krogstad, B. Dabrowski, and C. Leighton, Electrical transport, magnetic, and thermodynamic properties of la-, pr-, and nd-doped $BaSno_{3-\delta}$ single crystals, Phys. Rev. Mater. **2**, 084601 (2018).

[54] J. Wood, M. Howes, and D. Morgan, The effect of dislocations on the electron mobility of GaAs, Phys. Status Solidi A **74**, 493 (1982).

[55] J. You, J.-Q. Lu, and H. Johnson, Electron scattering due to threading edge dislocations in n-type wurtzite GaN, J. Appl. Phys. **99**, 033706 (2006).

[56] N. Miller, E. E. Haller, G. Koblmüller, C. Gallinat, J. S. Speck, W. J. Schaff, M. E. Hawkridge, K. M. Yu, and J. W. Ager, Effect of charged dislocation scattering on electrical and electrothermal transport in n-type InN, Phys. Rev. B **84**, 075315 (2011).

[57] D. Yoon, S. Yu, and J. Son, Oxygen vacancy-assisted recovery process for increasing electron mobility in n-type $BaSnO_3$ epitaxial thin films, NPG Asia Materials **10**, 363 (2018).

[58] S. Yu, D. Yoon, and J. Son, Enhancing electron mobility in La-doped $BaSnO_3$ thin films by thermal strain to annihilate extended defects, Appl. Phys. Lett. **108**, 262101 (2015).